EMi Taylor & Francis
Taylor & Francis Group

Thonningianin A disrupts pA104R−DNA binding and inhibits African swine fever virus replication

Quan-jie Li[a]#, Hui-han Shao[a]#, Lin-lin Zheng[b]#, Qian Liu[a], Chen-chao Huo[a], Dong-rong Yi[a], Tao Feng[b] and Shan Cen[a,c]

[a]Institute of Medicinal Biotechnology, Chinese Academy of Medical Sciences & Peking Union Medical College, Beijing, People's Republic of China; [b]State Key Laboratory for Animal Disease Control and Prevention, College of Veterinary Medicine, Lanzhou University, Lanzhou Veterinary Research Institute, Chinese Academy of Agricultural Sciences, Lanzhou, People's Republic of China; [c]CAMS Key Laboratory of Antiviral Drug Research, Peking Union Medical College, Chinese Academy of Medical Sciences, Beijing, People's Republic of China

ABSTRACT
African swine fever is a highly lethal disease caused by the African swine fever virus (ASFV), posing a significant threat to the global pig industry, wherease no approved treatments are currently available. The ASFV DNA-binding protein, pA104R, plays a critical role in viral genome packaging and replication, making it a key target for drug discovery. Through structure-based virtual screening, we identified a polyphenolic compound, thonningianin A, which disrupts the pA104R−DNA binding and significantly inhibits ASFV replication. Mechanistic study revealed that thonningianin A binds to the DNA-binding region of pA104R, forming strong hydrogen bonds with H100 and occupying the vital DNA-binding residues K92, R94, and K97. In addition, we resolved the high-resolution (1.8 Å) structure of pA104R (PDB ID 9JS5), providing valuable insights for future drug screening. Together, these results demonstrate that thonningianin A holds great potential for the development of anti-ASFV drug, as a herb extract with favourable pharmacokinetic properties and safety.
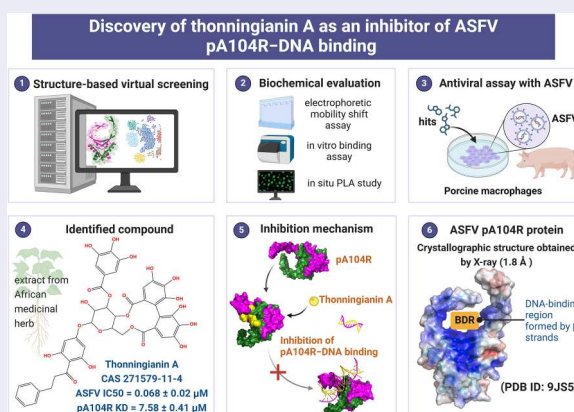
Discovery of thonningianin A as an inhibitor of ASFV pA104R−DNA binding

Introduction

African Swine Fever (ASF) is a highly contagious and fatal disease caused by the African Swine Fever Virus (ASFV), primarily affecting domestic pigs and wild boars [1]. High-virulence ASFV strains can cause acute hemorrhagic fever with a mortality rate of up to 100%, posing a severe threat to the global swine industry [2]. Since its first discovery in Kenya in 1921, ASF has spread to multiple regions worldwide, with significant increases in transmission in Europe and Asia since 2016 [3]. In August 2018, ASFV was detected for the first time in China, the world's largest pork producer, resulting in the culling of millions of pigs and substantial economic losses. Currently, there

are no safe and effective commercial vaccines or treatments available, except for a gene-deleted live attenuated vaccine (ASFV-G-ΔI177L) licensed exclusively in Vietnam [4–6]. Existing control strategies primarily rely on quarantine and culling of infected animals, which pose significant threats to the swine industry and food security. Therefore, there is an urgent need to develop new control strategies, including vaccines and antiviral drugs, to effectively respond to ASF outbreaks.

ASFV is the only member of the Asfarviridae family, belonging to the genus Asfivirus, and is the sole known DNA arbovirus [7]. Its genome consists of linear double-stranded DNA, varying in length from 170 to 193 kbp, and encodes 151–167 open reading frames (ORFs). The functions of approximately half of these genes are still unknown[2,8]. Recent advances have depicted the architecture of ASFV particles, revealing a diameter of approximately 250 nanometres and a quintuple-layered structure comprising an outer envelope, an icosahedral protein capsid, an inner membrane, a core shell, and a nucleoid [9–12]. This multilayer icosahedral configuration not only shields the genome from degradation by host cell nucleases but also facilitates various functions related to viral infection and transmission [13]. However, the structural complexity of ASFV poses substantial challenges for the development of vaccines and antiviral drugs, and also highlights the importance of identifying key antiviral targets.

As the only histone-like protein encoded by ASFV, pA104R serves as the primary DNA-binding protein and plays a crucial role in viral DNA replication, transcription, and genome packaging, making it an important target for diagnosis, treatment, and immunoprevention of ASFV [14,15]. pA104R consists of 104 amino acid residues, with a molecular weight of 11.6 kDa and an isoelectric point of 11 [16]. The monomeric structure of pA104R includes two α-helices (α1 and α2), five β-strands (β1-β5), and a terminal α/3_10 helix (α3/η1). In solution, it exists as a homodimer, featuring a body region composed of α-helices (AHR) and a DNA-binding region formed by β-strands (BDR) [17]. pA104R binds to single-stranded DNA (ssDNA) and double-stranded DNA (dsDNA) in an ATP-independent manner [15]. The dense positive charge of amino acids in its BDR is crucial for interaction with the negatively charged DNA backbone. The positively charged residues, including R69, H72, K92, R94, and K97, are essential for DNA-binding activity [18,19]. Compared to the residues in the arm region (R69 and H72), the three residues located in the bottom region (K92, R94, and K97) contribute more significantly to DNA binding [17].

Given the pivotal role of pA104R in ASFV, extensive efforts have been made to develop therapeutic interventions targeting this protein. However, attempts to develop vaccines based on pA104R have been unsuccessful [18,20,21], and there are currently no effective drugs available. Although previous studies have demonstrated that several small molecule inhibitors, such as stilbene derivatives (SD4, resveratrol, and oxyresveratrol), can disrupt ASFV infection by potentially inhibiting pA104R−DNA binding [17,22], the mechanisms of these drugs are not yet fully elucidated and await further validation [17]. Therefore, there is still a need for the development of drugs specifically targeting pA104R, which could also provide evidence supporting the feasibility of such target.

Currently, nucleoside analogs (Brincidofovir [23], cHPMPC [24], and cytarabine hydrochloride [25]), fluoroquinolone antibiotics such as enrofloxacin [26,27], and other synthetic small molecules, including brequinar [28,29], triapine [25], ARV-825 [30], BAY11-7082 [31], and E-64 [32], have demonstrated potent antiviral activity against ASFV. However, their high costs limit their widespread use in the swine industry. Consequently, research is increasingly focusing on economically feasible and readily available natural antiviral drugs. Host-targeting antivirals such as lauryl gallate [33], theaflavin [34], tetrandrine [35], dihydromyricetin [36], genkwanin [37], and kaempferol [38], disrupt host cell metabolism, signalling pathways, microtubule polymerization, and autophagy, showing notable antiviral activities. Furthermore, some natural products that target ASFV viral proteins, such as type II topoisomerase inhibitors genistein [39], arctiin, and genistein [40], as well as protease inhibitors myricetin and myricitrin [41], have shown effective antiviral properties. Additionally, natural products such as apigenin [42], ailanthone [43], lauryl gallate [44], tetrandrine [45] and berbamine [45] have also been reported to possess ASFV inhibitory activity, though their mechanisms remain unclear. Notably, natural products may possess potential toxicity and adverse effects, which require comprehensive safety evaluations [46].

In this study, using a structure-based virtual screening approach, we screened a collection of bioactive compounds, including those from a natural compound library, targeting pA104R. For compounds with favourable binding energy to pA104R, we evaluated their effects on pA104R−DNA binding using electrophoretic mobility shift assays (EMSA) and proximity ligation assays (PLA) at both in vitro and cellular levels. We identified a compound, thonningianin A, that inhibits pA104R−DNA binding and effectively suppresses ASFV replication. Further biological experiments, including binding site analysis and site-directed mutagenesis, elucidated its binding mode and mechanism of action. Although we were unable to obtain the co-crystal structure of pA104R and thonningianin A, we have resolved the highest-resolution crystal structure of pA104R to date (PDB ID 9JS5), providing more detailed and precise structural information for subsequent drug discovery efforts. Derived

from African herbal extracts, thonningianin A is cost-effective, easily accessible, and exhibits remarkable antiviral activity against ASFV at the cellular level, highlighting its potential as a broadly applicable antiviral drug for veterinary medicine.

Materials and methods

Structure-based virtual screening

For the virtual screening, the crystal structure of pA104R in complex with DNA (PDB ID 6LMJ) was chosen as the templates to provide an appropriate ligand-binding pocket. Docking parameters were generated using AutoDockTools(version 1.5.7) [47] based on the interface between pA104R and DNA. The active site was defined within a box with dimensions of 20.11 Å × −24.538 Å × −9.648 Å. The grid size for docking was set to 40, 50, and 40 Å along the X, Y and Z axex, respectively. The PDBQT file for ƚ pA104R was also prepared using AutoDockTools. This involved adding polar hydrogens to the protein PDB file, calculating Gasteiger charges, and saving the result in PDBQT format. For the small molecule ligands, hydrogen atoms were appended at pH 7.4 using Open Babel (version 2.3.2) [48], and the output structures were then saved as PDBQT files for dockings. Subsequently, a total of 37,551 compounds, sourced from the DrugBank database (version 5.1.5), TargetMol's natural compound library (Catalog No. L6020), and TargetMol bioactive compound Libraries (Catalog Nos. L1000, l3400, L4000, and L4150), were docked into pA104R using AutoDock Vina (version 1.2.0) [49]. During the docking process, we used a semi-flexible approach, treating the protein as rigid while allowing the ligands to be fully flexible. This approach was chosen to balance computational efficiency with accuracy, allowing ligands to explore various conformations within the defined binding site. The virtual screening (VS) results were ranked based on the predicted binding free energy (ΔG_{ADV}). The visualization and analysis of protein–ligand interactions were conducted using the PyMOL Molecular Graphics System (version 3.0.0) and Maestro (version 12.8.117).

Molecular dynamics simulation

The generated pA104R−compound46 complex structure obtained through molecular docking was further refined using molecule dynamics (MD) simulation. All simulations and analyses were conducted with the Amber11 software package. The Amber ff99SB force field was used to describe pA104R, and missing hydrogen atoms of the protein were added using the LEAP module. For the ligands, the preliminary topology and parameter files were parametrized with Antechamber from AmberTools, using the General Amber Force Field (GAFF). Quantum mechanical calculations were then performed using Gaussian 09 at the B3LYP/6-31G* level to derive restrained electrostatic potential (RESP) charges. These charges were then incorporated through Antechamber to update the topology file. Finally, parmchk was employed to generate the final force field parameter file (Supplementary Code 1).

A total of 17 Cl⁻ counterions were added to pA104R−compound46 complex for charge neutralization. The entire system was then solvated in a box of TIP3P water molecules extending 10 Å outside the protein. To obtain the appropriate geometry and avoid steric clashes, we performed a two-step energy minimization. The system was first minimized with the the pA104R−compound46 complex under 100 kcal/(mol·Å^2) constraints for 5000 steps, including 2500 steps using the steepest descent method and 2500 steps using the conjugate gradient method. After removing the constraints, the system was fully minimized for 10,000 steps, with 5000 steps using the steepest descent method and 5000 steps using the conjugate gradient method. Following this, the entire system was heated from 0 K to 300 K using Langevin dynamics, with a collision frequency (gamma_ln) of 1.0 ps^−1. The simulation ran for 50,000 steps with a time step of 2 fs. Periodic boundary conditions were used, and no pressure coupling was applied during the simulation (NVT). Positional restraints with a force constant of 10 kcal/(mol·Å^2) were applied to pA104R−compound46 complex to ensure its structural stability. Subsequently, the system was equilibrated for 500 ps at a constant pressure of 1 atm and temperature of 300 K (NPT). Finally, a production run of 50 ns simulations were performed with a time step of 2 fs under the same conditions. Throughout the simulation, the nonbonded interactions were evaluated with a cutoff of 10 Å, and the long-range electrostatic interactions were treated by Particle Mesh Ewald (PME) method. The SHAKE algorithm was applied to constrain the hydrogen bonds.

The structural stability and integrity of pA104R−compound46 complexes was analyzed by Root Mean Square Deviation (RMSD), Root Mean Square Fluctuations (RMSF) and intermolecular hydrogen bonds analysis. Representative structures of pA104R−compound46 complex were obtained through cluster analysis using the kclust module in MMTSB Tool Set. Binding free energy decomposition were calculated using the molecular mechanics/generalized born surface area (MM/GBSA) method. All the simulation results were visualized using VMD (version 1.9.3) and the PyMOL Molecular Graphics System (version 3.0.0).

Protein expression and purification

To express the wild-type pA104R (pA104R-WT) protein, the codon-optimized gene encoding residues

1–104 of pA104R (GenBank: AYW34006.1) was modified to include a His6-tag at the 5′ end and a stop codon at the 3′ end. It was then cloned into the BamHI and NotI sites of the pET-21a vector (Invitrogen). After transformation into the E. coli strain BL21 (DE3), the recombinant plasmid was cultured in LB medium under shaking conditions at 37°C until the optical density at 600 nm (OD600) reached 0.6∼1.0. The cultures were then induced with 0.5 mM isopropyl β-D-1-thiogalactopyranoside (IPTG) at 16°C for 16 h to promote the expression of the recombinant protein. After induction, the cells were harvested following 16 h and lysed by sonication in lysis buffer (20 mM Na_3PO_4, 500 mM NaCl, and 100 mM imidazole, pH 7.4). The recombinant protein was subsequently extracted from the lysate supernatant. After centrifugation, the supernatant was first purified using a HisTrap™ HP 5-mL column (GE Healthcare) through metal affinity chromatography. The protein was loaded onto the column with loading buffer (10 mM HEPES, 100 mM NaCl, pH 7.4) and eluted with elution buffer (10 mM HEPES, 100 mM NaCl, 500 mM imidazole, pH 7.4). To further enhance protein purity, the purified protein was first loaded onto a HiTrap™ QHP anion exchange column (GE Healthcare) with loading buffer (10 mM HEPES, pH 7.4), then eluted with elution buffer (10 mM HEPES, 1 M NaCl, pH 7.4). Finally, the protein was further purified by size exclusion chromatography using a Superdex™ 200 Increase PG column (GE Healthcare), equilibrated with binding buffer (10 mM HEPES, 100 mM NaCl, pH 7.4).

PCR-based site-directed mutagenesis

To construct the mutant protein, the plasmid pET-21a containing the pA104R gene fragment was used as the mutagenesis template, and primers containing mismatched bases were used for PCR amplification. The PCR reaction mixture included 50∼100 ng of template DNA, 20 μM of each primer, dNTPs, ddH2O, and DNA polymerase, with a total volume of 50 μL. The PCR amplification conditions were as follows: preheating at 98°C for 3 min; denaturation at 98°C for 30 s, annealing at 55°C for 30 s, and extension at 72°C for 5 min, for a total of 30 cycles, followed by incubation at 4°C. The PCR products were analyzed by agarose gel electrophoresis and purified using a PCR purification kit (Magen, China). The purified PCR products were then treated with the restriction enzyme DpnI (NEB) to degrade the template DNA. Next, 5 μL of the treated product was transformed into E. coli competent cells, which were then plated on LB agar containing 100 mg/mL ampicillin. Positive mutant colonies were selected through enzyme digestion screening to obtain the target mutant protein. The primer sequences are listed in Supplementary Table 1.

Electrophoresis mobility shift assay

5′ FAM-labelled single-strand oligonucleotides (Sequence (5′ to 3′): CCAACTTCCCTAACC-CAGCTGCGATCCGTA, 30nt) synthesized by AZENTA were dissolved in binding buffer (Beyotime, cat. # GS005). Corresponding double-stranded oligonucleotides were generated by annealing the 5′ FAM-labelled single strand with an unlabeled complementary strand (Sequence (5′ to 3′): TACGGATCG-CAGCTGGGTTAGGGAAGTTGG) at a 1:1 molar ratio.

pA104R−DNA binding reactions were conducted using EMSA/Gel shift kit (Beyotime, cat. # GS009). pA104R, serially diluted to target concentrations as shown in Supplementary Figure 1, was mixed with DNA (1 μM) and incubated at room temperature for 30 min. Subsequently, the reaction mixture was supplemented with 5 × loading buffer (Beyotime, cat. #GS006 and GS007) and electrophoresed in a 10% native polyacrylamide gel (PAGE) containing 0.5 × Tris-borate-EDTA (TBE). Following electrophoresis, the gel was visualized using the Bio-Rad imaging system.

For the small molecule inhibition assay, compounds were initially dissolved in dimethyl sulfoxide (DMSO) to make a 10 mM stock solution and then gradient diluted. To assess whether incubation order affects binding, we tested pre-incubating compounds with DNA before adding the protein and found no significant difference compared to simultaneous incubation. Therefore, all experiments in this study were conducted using simultaneous incubation, where different concentrations of compounds were incubated with 30 bp double-stranded DNA (1 μM) and pA104R protein (20 μM) simultaneously at room temperature for 30 min, followed by electrophoresis on a 10% native PAGE. After electrophoresis, images were analyzed with ImageJ software. In the experiments, DMSO served as the negative control and SD4 as the positive control.

BLI binding assay

The binding kinetics between WT or mutant pA104R proteins and selected compounds were determined using the Octet RED96 system (ForteBio, Inc.). The experiment was conducted at 30°C with a shaking speed of 1000 rpm. His-tagged WT or mutant pA104R proteins (∼160 μg/mL) were loaded onto Ni-NTA (NTA) biosensors (Cat #: 18-5101, Sartorius), and the loading was continued for 90 s until the loading curve reached saturation. During the KD determination, the biosensor tips were immersed in wells containing compounds diluted in a 2-fold series from 100 μM to 6.25 μM. Each analysis cycle included a baseline collection for 60 s, a compound association

phase for 180 s to determine the association rate constant (kon), and a dissociation phase in buffer for 180 s to measure the dissociation rate constant (koff). Independent sensors were used for each concentration of the compound. The assay buffer consisted of PBS with 2% DMSO. To correct for baseline drift, an empty well containing only the buffer was used for blank binding cycles. Additionally, reference sensors that were not loaded with protein were incubated in buffer alone to monitor non-specific binding. Baseline drift and non-specific binding were eliminated using dual reference subtraction. The kinetic parameters were calculated using a 1:1 global fit model, with the Rmax unlinked by sensors, analyzed using the Octet data analysis software (ForteBio, version 9.0).

Crystallization and data collection

The pA104R was crystallized using the hanging-drop vapour diffusion method with 1 μL protein (13.53 mg/mL) mixed with 1 μL reservoir solution and then equilibrating against 100 μL reservoir solution at 18°C. Initial crystallization condition of pA104R-apo were referred from PDB: 6LMH. Qualified crystals of pA104R-apo were obtained with a reservoir solution of 2.6 M ammonium sulfate, 0.1 M citric acid, pH 4.0 within 2 days. To obtain the complex of pA104R bound to compound via soaking, the pre-formed pA104R crystals were incubated in the reservoir solution supplemented with 2.5 mM compound at 18°C for 18 h.

Considering the potential interference of sulfate ions in the reservoir solution on the co-crystallization of the pA104R and compound, we also explored sulfate-free crystallization conditions using a crystallization screening kit. pA104R-apo protein (12.6 mg/mL) was mixed with a dsDNA at a molar ratio of 1:5, and simultaneously with compound at a molar ratio of 1:2. The mixture was incubated on ice for 2 h to form a complex. Subsequently, co-crystallization was carried out using the sitting-drop vapour diffusion method with 0.2 μL mixture combined with 0.1 μL reservoir solution, and then equilibrating against 30 μL reservoir solution at 18°C. The initial crystallization conditions were identified using the Morpheus Kit H4 protein crystallization kit (Molecular Dimensions). To further optimize crystal growth, the Additive Screen Kit A4 (Hampton Research) was employed. The final crystals were obtained after 4 weeks of incubation in a reservoir solution containing 0.1 M amino acids, 0.1 M (Imidazole/MES) pH6.5, 12.5% v/v MPD,12.5% w/v PEG1000, 12.5% w/v PEG 3350, and 0.1 M cadmium chloride hydrate.

For data collection, the crystals were flash-cooled in liquid nitrogen after a brief soaking in reservoir solution with the addition of 20% (vol/vol) glycerol. Diffraction data were collected on the beamline BL19U1 at the Shanghai Synchrotron Radiation Facility (SSRF, Shanghai, China). Diffraction was performed using a λ = 0.97851 Å wavelength. Diffraction data sets were processed using the programme XDS and AIMLESS from the CCP4 suite.

Structure determination

The structure was solved by the molecular replacement method using Phaser from the CCP4 programme suite with the solved pA104R structure (PDB ID 6LMH) as the search model. The initial model was constructed using the Autobuild feature in the Phenix suite [50], after which missing residues were manually inserted using COOT [51]. The atomic model was subsequently completed in COOT and refined using phenix.refine. The stereochemical quality of the final models was evaluated with MolProbity. All structural figures were generated using the PyMOL Molecular Graphics System (version 3.0.0).

In situ proximity ligation assay (PLA)

PLA were conducted using Duolink® In Situ PLA reagents (Sigma Aldrich, #DUO92008). Briefly, Vero cells were co-transfected with plasmids expressing pA104R and dsDNA for 48 h, with compounds added prior to transfection. After treatment, cells were fixed with 4% paraformaldehyde for 15 min, permeabilized with 0.2% Triton X-100, and blocked with the blocking solution provided in the kit for 1 h. Subsequently, cells were incubated with primary antibodies (anti-flag tag antibody (1:1000, Cell Signalling Technology, #8146S) and anti-dsDNA antibody (1:1000, Abcam, #270732)) at room temperature for 1 h. Following incubation, cells were washed with buffer A (10 mM Tris, 150 mM NaCl, 0.05％Tween20) and incubated with secondary antibodies conjugated with Duolink PLA PLUS and MINUS probes at 37 °C for 1 h. The ligase and polymerase were diluted in $1 \times$ ligation buffer and $1 \times$ amplification buffer, respectively. Cells were then incubated with the ligase at 37°C for 30 min, followed by incubation with the polymerase at 37°C for 100 min. Finally, samples were washed with buffer B (200 mM Tris, 100 mM NaCl) and stained with DAPI. Fluorescence signals were recorded by a PerkinElmer Ultra View VoX confocal microscope using a 100× oil objective. Red spots indicate the binding between pA104R and dsDNA.

Cells and viruses

Primary porcine alveolar macrophages (PAMs) were collected using bronchoalveolar lavage as described

previously and cultured in Roswell Park Memorial Institute (RPMI) 1640 Medium (Gibco) supplemented with 10% fetal bovine sera (Gibco), 200-mg/mL streptomycin, and 200-IU/mL penicillin at 37°C. Vero E6 (ATCC, CRL-1586), Huh7.5.1 (Rongtuan Lin, McGill University), and BHK-21 (C-13, ATCCCCL-10) cell lines, were cultured in Dulbecco's modified Eagle medium (DMEM) supplemented with 100 μg/mL streptomycin, 50 U/mL penicillin, and 10% FBS. All cell lines were incubated at 37°C with 5% CO2.

ASFV CN/GS/2018 was provided by the Lanzhou Veterinary Research Institute, Chinese Academy of Agricultural Sciences. All experiments with live virus were conducted in biosafety level 3 facilities in the Lanzhou Veterinary Research Institute of the Chinese Academy of Agricultural Science.

In vitro antiviral assay

PAMs were seeded into 24-well plates (1×10^5 cells/well) and cultured for 12 h. Following this, the cells were infected with ASFV CN/GS/2018 at a multiplicity of infection (MOI) of 0.01 for 1 h. After the infection, the culture medium was replaced with fresh RPMI 1640 medium containing test compounds at various concentrations, diluted 10-fold from 40 μM to 0.4 nM. The cells were then incubated for an additional 48 h. To assess the impact of the different concentrations of compounds on ASFV genome expression, relative quantification methods were employed. DNA was extracted from the treated cells using QIAamp DNA Mini Kit (Qiagen, Germany). The VP72 gene of the ASFV genome was specifically amplified using the real-time PCR method. The primers used were as follows: the forward primer 5′-CTGCTCATGGTATCAATCTTATCGA-3′ and the reverse primer 5′-GATACCACAAGATCAGCCGT-3′. A TaqMan probe 5′-CCACGGGAGGAATAC-CAACCCAGTG-3′ was employed to enhance specificity and allow for the quantification of the viral genome. Real-time PCR was conducted using the Pro Taq HS Premix Probe qPCR kit (Accurate Biology, China) on a QuantStudio 3 Real-Time PCR System (Applied Biosystems, USA), adhering strictly to the manufacturer's protocol.

Cytotoxicity analysis

Cells were cultured in 96-well plates at 37°C for 24 h, after which the tested compounds were added. The cells were then incubated for 48 h under conditions of 37°C and 5% CO₂, with DMSO serving as a negative control. After incubation, cell viability was assessed using the Cell Counting kit-8 (Cat #40203ES92, Yeasen, China), and optical density (OD) at 450 nm were measured using a microplate reader (Thermo, Varioskan Flash).

Statistical information

All in vitro experiments were performed at least three times. Data are presented as the means ± standard error of the mean (SEM) unless otherwise stated. Statistical significance was calculated using one-way analysis of variance (ANOVA) followed by Dunnett's multiple comparisons test or two-way ANOVA followed by Sidak's multiple comparisons test for pairwise analysis. All the statistical analyses were performed using GraphPad Prism version 10.0.0, GraphPad Software, Boston, Massachusetts USA, www.graphpad.com.

Results

Virtual screening of the small compound libraries against pA104R

The ASFV-encoded pA104R protein, located in the nucleoid, is a DNA binding protein involved in viral DNA replication. Inhibitors that are capable of interrupting the pA104R−DNA binding would potentially inhibit ASFV replication. The crystal structure of pA104R in complex with DNA (PDB ID 6LMJ) was chosen as the template to provide suitable ligand binding pockets for virtual screening (VS). A total of 37,551 compounds from DrugBank, Natural Compound Library, and TargetMol Bioactive Compounds Library were docked into pA104R (Figure 1(a)). The VS results were sorted on the basis of their predicted binding free energies (ΔG_{ADV}), which ranged from −9.6 to −0.6 kcal/mol (Figure 1(b)). Stilbene derivative SD4, known to inhibit the binding of dsDNA to pA104R [17], was docked into the pA104R−DNA interface by using the similar procedure. The results indicate that SD4 binds to the bottom region, exhibiting a ΔG_{ADV} values of −7.6 kcal/mol. To identify compounds that bind more strongly or comparably to SD4, we visually inspected compounds with binding energies more favourable than −7.6 kcal/mol. Considering the important roles of residues K92, R94, and K97 in contributing to the majority of the pA104R−DNA binding [17], compounds that exhibited H-bond or salt bridge interactions with these residues were preferentially selected during the visual inspection process. Finally, 50 purchasable compounds were obtained from TargetMol (Topscience, Shanghai, China), including 25 natural products. This ensures a diverse representation of both natural and synthetic compounds, enhancing the chemical variety of the screening. Their database ID, CAS number, name, formula, molecule
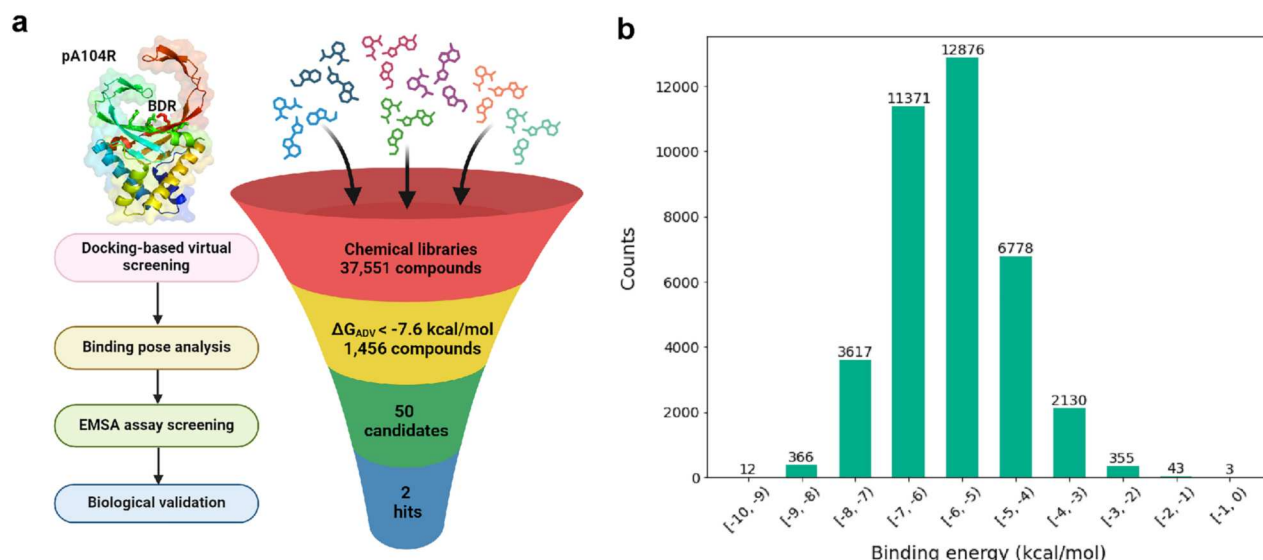
Figure 1. Structure-based discovery of small molecules targeting the β-strand DNA binding region (BDR) of pA104R. **a** Flowchart of the structure-based hierarchical virtual screening process. The figure was generated using BioRender.com. **b** Diverse binding energy levels exhibited by compounds in chemical libraries. Bars represent numbers of compounds with predicted free energies of binding in the indicated 1 kcal/mol bins.

weight (MolWt), and calculated binding energy (ΔG_{ADV}) are listed in Supplementary Table 2.

The inhibitory effect of selected compounds on pA104R−DNA binding

We employed EMSA to evaluate the inhibitory potential of 50 small molecules on pA104R−DNA binding, as previously described [15,17]. We first expressed and purified recombinant pA104R, which was confirmed to exist as a ∼12 kDa monomer on SDS-PAGE. Next, we evaluated the DNA binding ability of pA104R by incubating it with 30-nucleotide single-stranded DNA (ssDNA) and double-stranded DNA (dsDNA), each labelled with 5′-FAM. EMSA demonstrated its binding ability to both dsDNA and ssDNA. A dose–response study suggested 1 μM DNA and 10∼20 μM pA104R were optimal for further experiments (Supplementary Figure 1).

Based on this, we evaluated 50 compounds for their ability to inhibit pA104R−DNA binding using EMSA. Each compound (100 μM) was incubated with dsDNA and pA104R simultaneously for 30 min at room temperature. SD4, a known inhibitor of pA104R−DNA binding, was used as a reference. EMSA results showed that compounds 1 and compound 46 significantly reduced the binding affinity between DNA and pA104R, with an inhibition rate of approximately 90% (Figure 2(a)). We further examined the dose-dependent inhibitory effects of the compounds. As shown in Figure 2(b and c), compound 1 reduced the binding by 90% at a concentration of 50 μM and enhanced its inhibitory effect to 100% at 100 μM. Compound 46 achieved a 80% inhibition at the

100 μM concentration. The positive control compound SD4, exhibited an inhibitory effect only at 100 μM, with an inhibition rate ranging from 60% to 80%. These data indicate that both compound 1 and compound 46 can serve as effective inhibitors of the pA104R−DNA binding.

Next, we used BLI assays to evaluate their binding ability to pA104R in vitro. As shown in Figure 2(d–e), compound 1 and compound 46 exhibit strong binding to the target protein, with the KD values of 0.33±0.01 μM and 7.58±0.41 μM, respectively. Notably, compound 1 and compound 46 represent two distinct classes of compounds. Compound 1 is a sodium salt that possess negative charges in solution, whereases compound 46 is a neutral molecule characterized by a high hydroxyl group content (Figure 2(f and g)). Given that the pA104R−DNA binding interface is characterized by a high concentration of positively charged residues, it favours stronger electrostatic interactions with the negatively charged compound 1, as reflected in their lower KD values. Overall, the binding results suggests that these candidate compounds inhibit pA104R−DNA binding by interacting with pA104R.

Thonningianin A inhibits the replication of ASFV

Given that both compound 1 and compound 46 exhibit notable inhibitory effects on pA104R−DNA binding, their safety profiles were carefully evaluated to inform compound selection for further investigation. Compound 1 (evans blue), an azo dye widely used in biomedicine applications as a stain for cell and tissue death has been reported to have carcinogenic
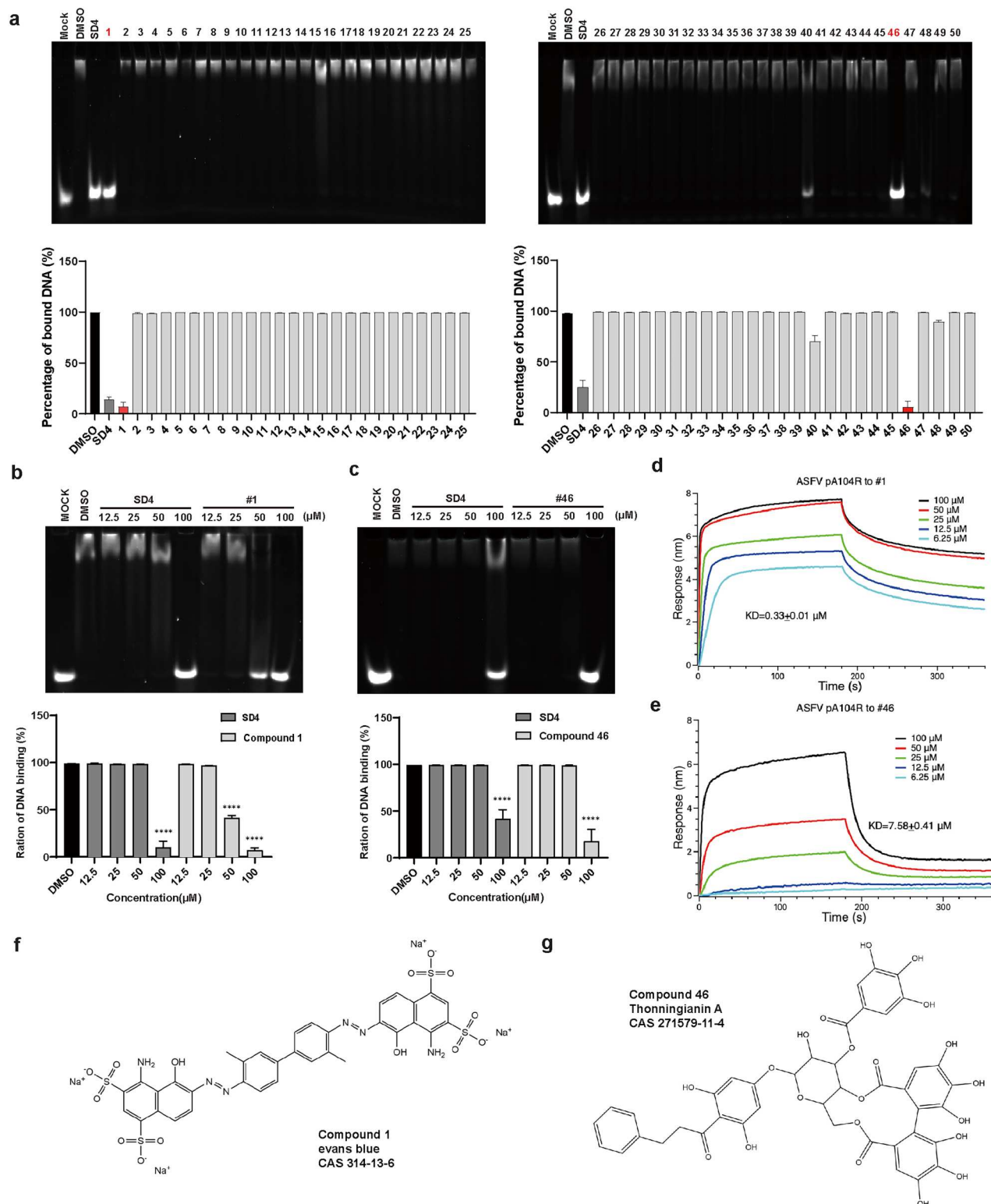
Figure 2. Identification of small molecules that inhibit pA104R−DNA binding using the EMSA method. a The effects of the screened 50 candidate compounds on the inhibition of pA104R−DNA binding in EMSA. DMSO was added as negative control and SD4 as positive control. The percentage of pA104R−DNA binding was analyzed by ImageJ software. The data are presented as the mean ± SD from three independent experiments. **b−c** The dose-dependent effects of compound 1 and compound 46 on the inhibition of pA104R−DNA binding in EMSAs. The data are presented as the mean ± SEM from three independent experiments. *P*-values were calculated using a one-way ANOVA followed by pairwise comparisons with Dunnett's multiple comparisons test, with DMSO as the control. ****$P < 0.0001$. For clarity, only significant correlations are shown. **d−e** BLI measurement of the binding between active compounds and pA104R. His-tagged WT pA104R was immobilized on NTA biosensors, and incubated with compounds diluted in a 2-fold series from 100 μM to 6.25 μM. Double reference subtraction method was processed to subtract the effect of baseline drift and non-specific binding. The kinetic parameters were calculated using a 1:1 global fit model, and analyzed using the Octet data analysis software (ForteBio, version 9.0). Data shown are representative of three independent experiments. **f−g** The 2D chemical structure of compound 1 and compound 46.
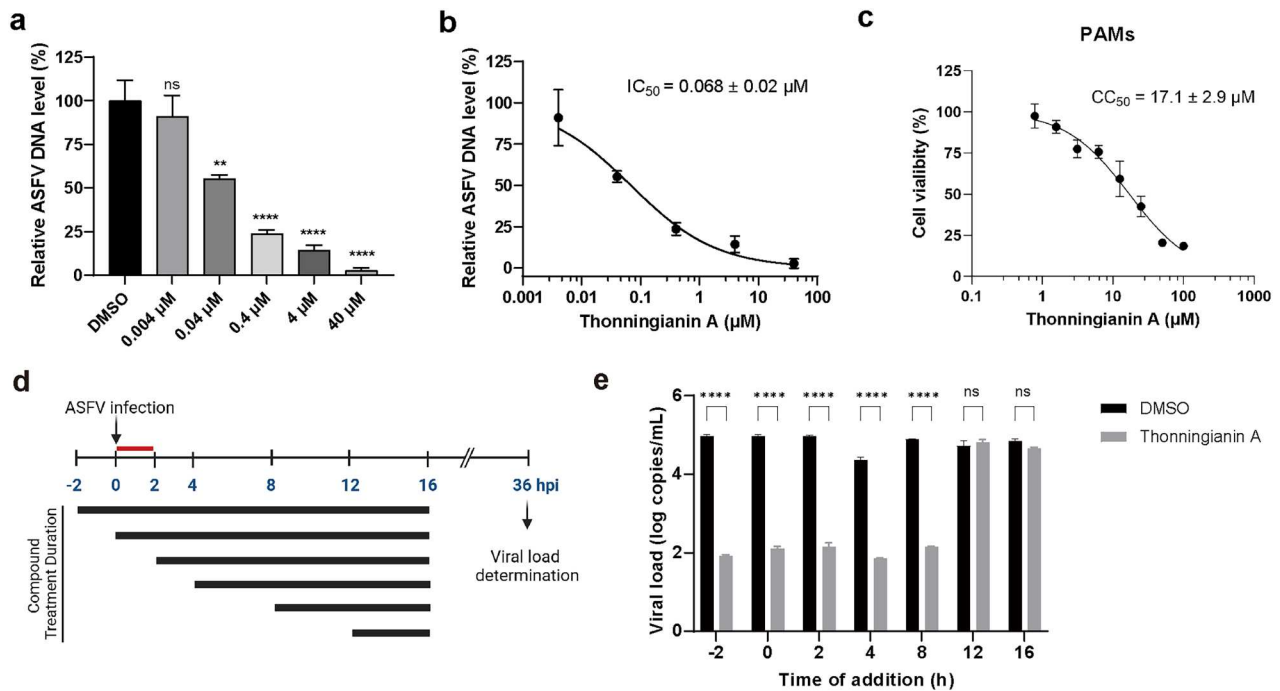
Figure 3. Inhibition of ASFV replication by thonningianin A. The inhibitory effects of thonningianin A on ASFV replication, as reflected by reductions in ASFV DNA levels **(a, b)**. DNA was extracted from treated cells, and the VP72 gene was amplified using qPCR. The relative DNA levels were determined by normalizing the viral copy numbers in the test wells to the mean viral copy number in the negative control wells (DMSO), which was set to 100%. Data are presented as the mean ± SEM from three independent experiments. **** $p < 0.0001$; *** $p < 0.001$; ** $p < 0.01$; ns = not significant, as determined by a one-way ANOVA followed by pairwise comparisons with Dunnett's multiple comparisons test, with DMSO as the control. **c** Cytotoxicity evaluation of thonningianin A in PAMs. Data are presented as the mean ± SD from three independent experiments. **d** Schematic illustration of time-of-addition experiment. PAM cells were infected with ASFV (MOI: 0.1) for 2 h. Thonningianin A (4 μM) was introduced at different time points. The viral genome copies were determined at 36 hpi by qPCR. **e** The effects of thonningianin A added at different time points on the viral genome copies. Data are presented as the mean ± SEM from three independent experiments. Statistical analysis was performed with two-way ANOVA, followed by Sidak's multiple comparisons test for pairwise analysis. **** $p < 0.0001$; ns, no statistical difference.

properties [52], thereby limiting its suitability for therapeutic development. In contrast, compound 46 (thonningianin A), a plant-derived antioxidant with potent anticancer and antioxidant activities, shows multiple biological properties with a higher safety profile. Therefore, we opted to focus on thonningianin A for further research.

We evaluated its ability to inhibit ASFV replication in swine macrophages. The impact of these compounds on viral production was quantitatively analyzed using real-time qPCR. As shown in Figure 3, thonningianin A markedly suppressed ASFV DNA levels in a dose-dependent manner, with an IC$_{50}$ value of 0.068 μM. Afterwards, we examined the cytotoxicity of it in PAMs and observed a favourable selectivity index (SI, CC$_{50}$/EC$_{50}$) of 251, indicating a substantial in vitro safety margin. To further assess its safety profile, we examined its cytotoxicity in Vero, Huh7.5.1, and BHK-21 cells. The CC$_{50}$ values were determined to be 10.6, 20.2 and 11.9 μM, respectively (Supplementary Figure 2). These results reveal a similar cytotoxicity across cell types. While in vivo safety requires further evaluation, the current data suggest its potential as a safe and effective antiviral candidate against ASFV.

To explore the stage of the viral replication cycle targeted by thonningianin A, we performed a time-of-addition assay in PAMs (Figure 3(d)). As shown in Figure 3(e), thonningianin A significantly inhibits ASFV replication even when added at 8 hpi, with a marked reduction in viral genomic DNA compared to the DMSO group ($10^{4.89}$ copies/mL vs $10^{2.15}$ copies/mL). Interestingly, the inhibitory effect observed at 8 hpi is comparable to that seen at earlier time points. We hypothesize that the early stages of viral infection may not be the primary target of this compound. While other potential mechanisms cannot be excluded, these results indicate that it targets the mid-stage of the viral lifecycle.

Blocking pA104R−DNA binding with thonningianin A: an in situ PLA study

To investigate the potential antiviral mechaims of thonningianin A, we first employed PLA to explore its ability to disrupt the pA104R−DNA binding at the cellular level. As shown in Figure 4, in the DMSO-treated control group, single-stranded DNA molecules labelled with FAM fluorescent dye
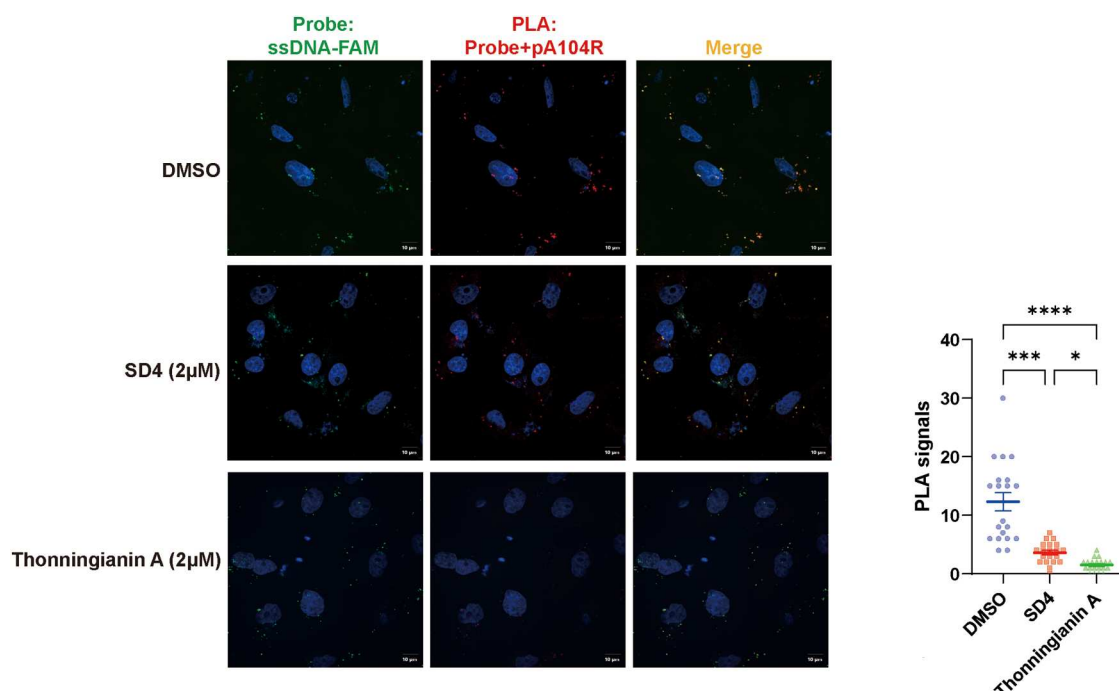
Figure 4. **Detection of pA104R−DNA binding by Proximity Ligation Assay in the presence of the compounds**. (left) Duolink proximity ligation assay for pA104R−DNA binding in Vero cells. The cells were treated with SD4 (2 µM) or compound 46 (2 µM), and then a Duolink assay was performed as described, with untreated cells serving as negative controls. Association of pA104R with DNA was detected as red puncta within cells. Representative images are shown, with experiments performed in triplicate. Nuclei were counterstained with DAPI (blue). Bars, 10 µm. (right) Red puncta were quantified in randomly selected cells ($n = 20$) using Image-Pro Plus 7.0 software (Media Cybernetics, USA). Data are presented as the mean of 20 cells per condition, collected from three independent biological replicates ($n = 3$), with error bars representing ± SEM. Statistical significance was determined using nonparametric Kruskal–Wallis one-way ANOVA on ranks, followed by Dunn's multiple comparison test. ***$p < 0.001$; ****$p < 0.0001$.

exhibited green fluorescence signals (Figure 4, top-left). When pA104R bound to DNA, red fluorescence signals were generated (Figure 4, top-center). Merged image resulted in predominantly yellow-orange (red plus green) (Figure 4, top-right), indicating a close spatial proximity or binding between DNA and pA104R. Upon addition of SD4 (2 µM), red fluorescence signals from the pA104R−DNA binding were still observed (Figure 4, middle-center). The merged image showed not only yellow-orange points but also green fluorescence spots, indicating the presence of DNA molecules not bound to pA104R. This suggests that SD4 partially blocks the pA104R−DNA binding. In the presence of thonningianin A (2 µM), the red fluorescence spots indicating pA104R−DNA binding almost disappeared (Figure 4, bottom-center). The merged image was predominantly green (Figure 4, bottom-right), indicating that thonningianin A effectively disrupts the pA104R−DNA binding. We further evaluated the impact of thonningianin A on pA104R expression (Supplementary Figure 3). The results showed that this compound did not alter protein expression levels, ruling out the possibility that thonningianin A inhibits pA104R−DNA binding by affecting the expression of pA104R.

Computational analysis of the pA104R−thonningianin A interactions

Subsequently, we investigated the interaction pattern between thonningianin A and pA104R through theoretical modelling. Thonningianin A was docked into the RBD region of pA104R to obtain the initial complex structure, which was then relaxed through a 50 ns MD simulation (Figure 5(a)). RMSF analysis showed that residues 66–85, in the β2–β3 fold region, exhibit high flexibility with values above 3 Å (Figure 5(b)). However, since this region is located at the end of the Arm domain and is distant from the compound binding site, it has little effect on the dynamical stability of the complex. Therefore, we calculated the RMSD values for the pA104R excluding these regions, and assessed the RMSD values for thonningianin A. The results showed that the RMSD values for both the pA104R and thonningianin A stabilized at 2 Å (Figure 5(c)), confirming the high stability of the complex structure.

Based on the MD simulation trajectory, we determined representative complex structures using cluster analysis and subsequently identified key hydrogen bond interactions through H-bond network analysists. Figure 5(d) shows that thonningianin A is situated at the bottom of pA104R BDR, interacting with amino
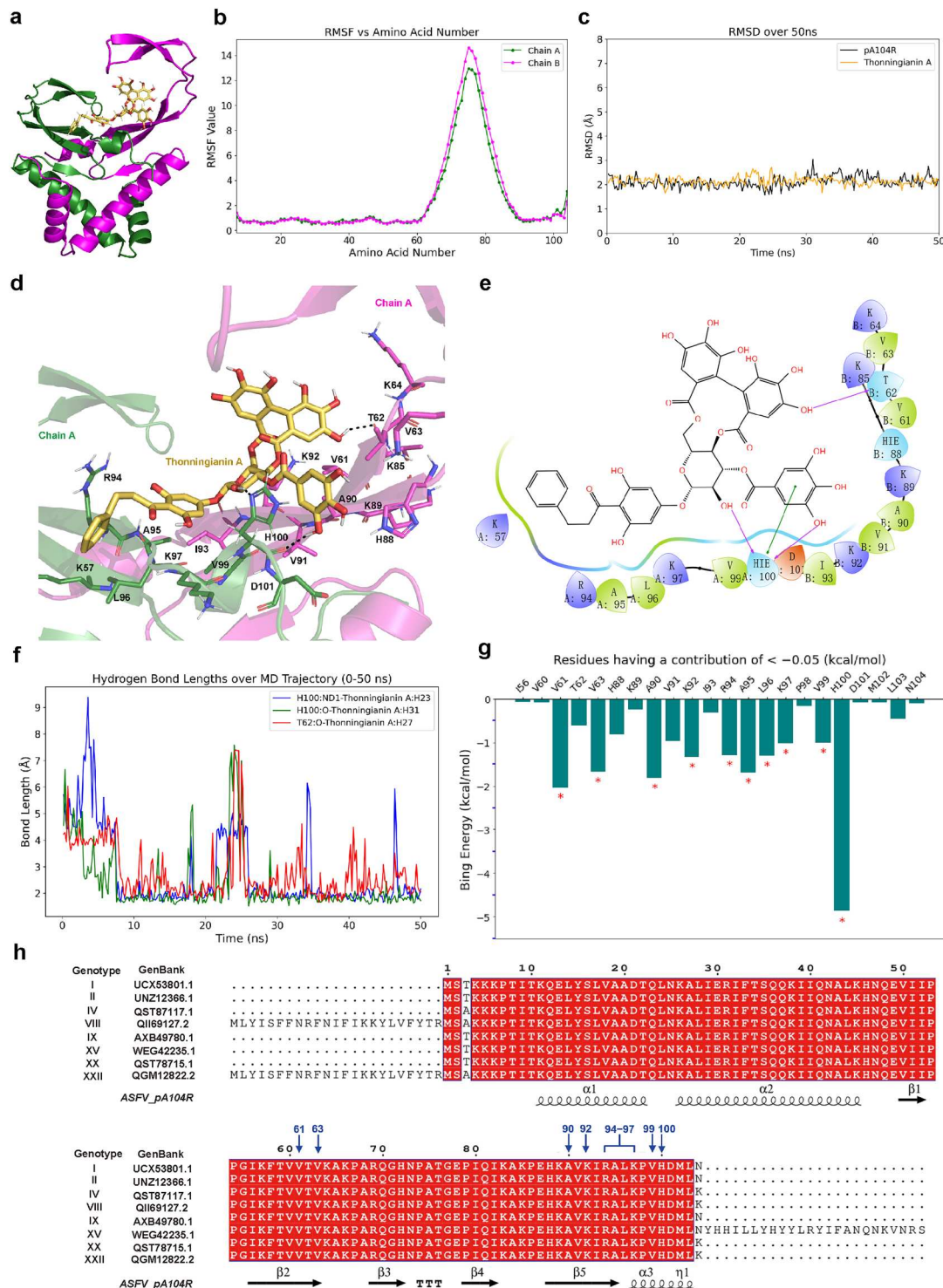
Figure 5. Computational analysis of the binding mode of thonningianin A to pA104R. a Representative structure of pA104R–thonningianin A obtained from clustering analysis of the MD trajectories. The pA104R protein is displayed in a cartoon representation, with the backbone atoms of chain A depicted in green and those of chain B in magenta. The ligand is displayed in yellow sticks. **b** RMSF of Cα atoms relative to the average structure of pA104R. **c** The RMSD values for thonningianin A-bound pA104R system along the MD simulation time. Black curves represent the RMSD values of pA104R backbone atoms (excluding the highly flexible terminal tail residues 66-85), whereas the yellow lines represent the RMSD curve of compound 46 heavy atoms. **d** Predicted binding pose of thonningianin A in pA104R. compund and the amino acid residues involved the protein-ligand interactions are shown as sticks. Hydrogen bonds are depicted as black dotted lines. **e** The 2D ligand-protein interaction diagrams. Residues within 5 Å of thonningianin A are displayed. Hydrogen bonds are represented by magenta arrows, and π-π stacking is marked in green. Dark blue indicates positive charge, red indicates negative charge, light blue for polar, and green for hydrophobic. **f** Distance of H-bond trajectories during MD simulation. **g** Residue-wise energy decomposition analysis. The diagram displays residues with a total energy contribution of ≤ −0.05 kcal/mol. The top ten amino acids contributing most significantly to the ligand binding are labelled with red asterisks (*). **h** Multiple sequence alignment of pA104R across different ASFV genotypes. The alignment was performed using ClustalW, and conservation levels were visualized with ESPript 3.0. The predicted critical binding residues of thonningianin A are highlighted by blue arrows.

acids on chains A and B. Binding mode analysis (Figure 5(e)) reveals that H100 forms two strong hydrogen bonds with thonningianin A. Specifically, the Nε2 atom and the backbone oxygen of H100 each interact individually with different hydroxyl groups of thonningianin A. During the 50 ns simulation, the occupation rates of these hydrogen bonds are 72.8% and 62.8%, with average bond lengths of 2.7 and 2.8 Å, respectively (Figure 5(f)). Additionally, H100 engages in π-π interactions with the pyrogallol group of thonningianin A. In addition, the backbone oxygen of T62 also forms a hydrogen bond with the hydroxyl group of thonningianin A, with an occupation rate of 40.4% and an average bond length of 2.8 Å during the simulation (Figure 5(f)). Besides hydrogen bonding, V63, V61, A90, V91, I93, V99, L96, and A95 form hydrophobic interactions with thonningianin A, while K57, R94, K97, K92, K89, K85, and K64 form electrostatic interactions with the compound.

To identify key amino acids critical for binding thonningianin A, we employed the MM/GBSA method to analyze the binding free energy contributions of individual residues. Figure 5(g) presents residues with binding free energy contributions greater than −0.5 kcal/mol, with the top 10 residues highlighted by asterisks: H100 (−4.874 kcal/mol), V61 (−2.04 kcal/mol), A90 (−1.82 kcal/mol), A95 (−1.69 kcal/mol), V63 (−1.67 kcal/mol), K92 (−1.34 kcal/mol), L96 (−1.30 kcal/mol), R94 (−1.29 kcal/mol), K97 (−1.02 kcal/mol), and V99 (−1.00 kcal/mol). Additionally, Supplementary Figure 4 decomposes the total binding free energy into its individual contributing components. The analysis reveals that, in addition to previously discussed electrostatic interactions and non-polar solvation energy, van der Waals interactions also play a crucial role in stabilizing the pA104R−thonningianin A complex.

Multiple sequence alignment of pA104R across different ASFV genotypes revealed that the critical binding residues (highlighted by blue arrows) are identical across all genotypes (Figure 5(h)), suggesting that Thonningianin A may possess broad-spectrum antiviral potential. Given the high conservation of these key binding residues, it is essential to evaluate their spatial relationship with the functionally important domain of pA104R, specifically the DNA-binding region. Superimposition of the pA104R−DNA complex with our predicted pA104R−thonningianin A complex shows that thonningianin A binds at the bottom region of the DNA binding site (Supplementary Figure 5). Among the residues involved in DNA binding, K57, K85, K92, R94, L96, K97 also interact with thonningianin A. The presence of shared key residues implies potential competition, where thonningianin A may interfere with DNA binding to pA104R.

Experimental validation of predicted pA104R–thonningianin A interactions

To validate the predicted binding sites of thonningianin A, we conducted site-directed mutagenesis experiments targeting the hot spot residues identified through binding free energy decomposition analysis. Considering the presence of positively charged amino acids in the binding cavity, we concentrated on evaluating the impact of polar interactions and charges on the stability of the binding site. We specifically mutated H100, which forms two stable hydrogen bonds with the compound, along with three other positively charged amino acids, including K92, R94, and K97, that engage in polar interactions with the compound. The other amino acids, such as V61, V63, A90, A95, L96 and V99, that predominantly engage in hydrophobic interactions with the compound, were excluded from the experiments. Specifically, we mutated each of these positively charged residues (K92, R94, K97, and H100) individually to aspartic acid (D), changing the positively charged residues to negatively charged ones. Additionally, H100 was also mutated to alanine (A) to specifically investigate the effect of eliminating the hydrogen bonds formed by its side chain with the compound.

Following the purification of pA104R mutants, we utilized EMSA to examine whether mutations could impact the compound's ability to inhibit pA104R−DNA binding. As illustrated in Figure 6(a–e), thonningianin A exhibits approximately 60%∼80% inhibition of the binding between the wild-type pA104R and DNA at a concentration of 100 μM. When residues K92, R94, K97, and H100 were mutated to D, the binding between the mutated pA104R and DNA remained unaffected, as observed in the DMSO control groups. However, the compound was no longer able to inhibit their interaction at the same concentration. This suggests that the reduced inhibitory effect of the compound may be attributable to its impaired interaction with the mutant protein, rather than the changes in the binding affinity between the mutant protein and DNA. A similar phenomenon was observed with the H100A mutation.

To further validate these key binding sites, we used BLI technology to measure the binding affinity between thonningianin A and the mutant proteins. As shown in Figure 6(f–j), the KD values for K92D, R94D, K97D, H100D, and H100A are 53.07 μM, 33.88 μM, 23.37 μM, 31.82 μM, 38.62 μM, respectively. Compared to the wild-type protein (WT; KD = 7.58 μM), the binding affinities of these mutants are weakened to varying degrees, with relative fold-changes ranging from 3.1-fold to 7.0-fold (Supplementary Table 3). While the single-point mutations in these variants allow them to retain moderate affinity for thonningianin A, their weakened binding abilities
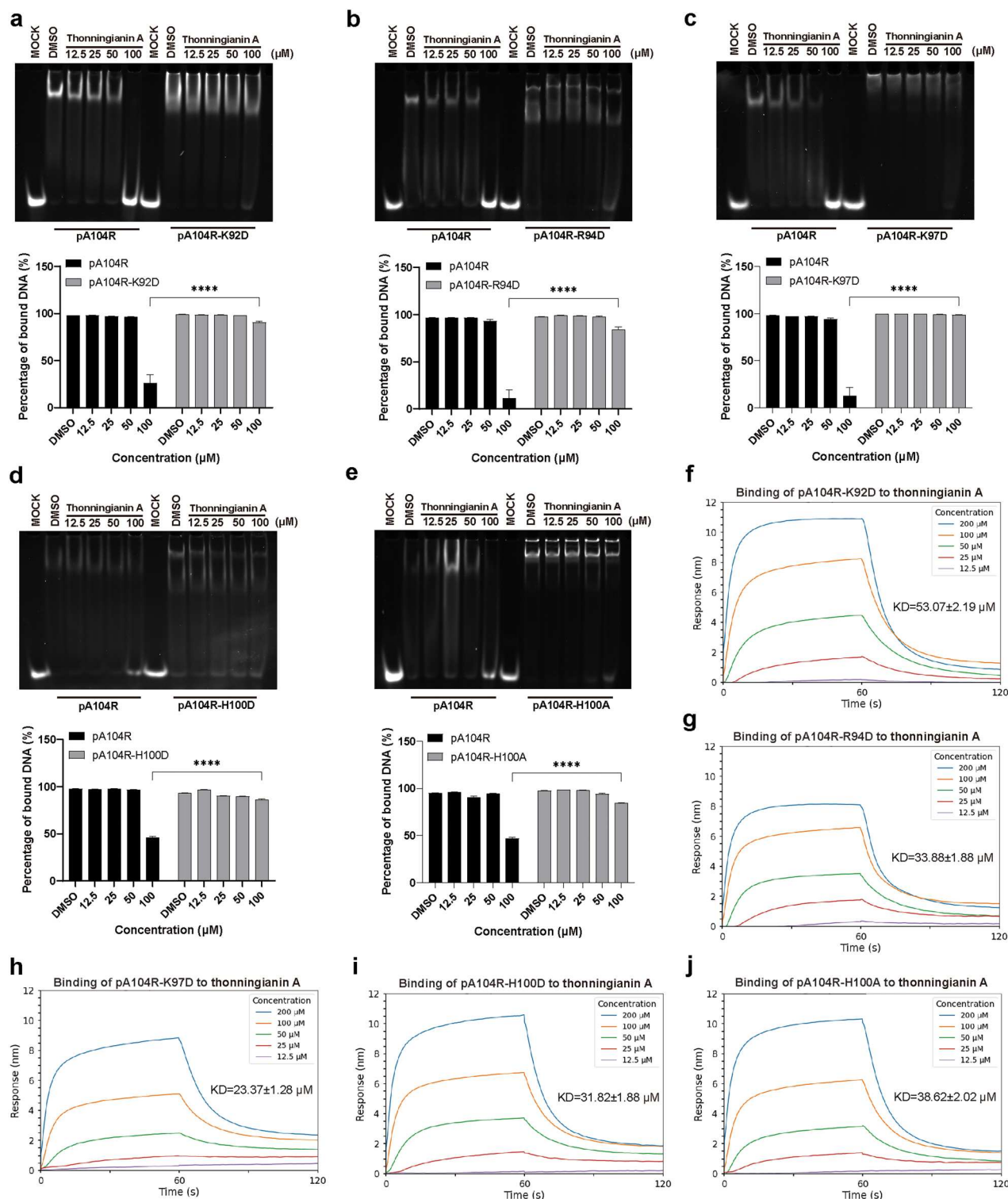
Figure 6. Validation of the potential binding sites of thonningianin A through hotspot mutations and EMSA analysis. (**a–f**) Effects of thonningianin A on the inhibition of DNA binding to K92D (**a**), R94D (**b**), K97D (**c**), H100D (**d**), and H100A (**e**) mutants in EMSAs. The wild-type pA104R was used as a control. The data are presented as the mean ± SEM from three independent experiments. *P*-values were calculated using a two-way ANOVA followed by Sidak's multiple comparisons test for pairwise analysis. ****$P < 0.0001$. For clarity, only the comparisons at the highest concentration are shown. (**f–j**) The binding dynamics between K92D (**f**), R94D (**g**), K97D (**h**), H100D (**i**), and H100A (**j**) and compound46, respectively. Double reference subtraction method was processed to subtract the effect of baseline drift and non-specific binding. The kinetic parameters were calculated using a 1:1 global fit model, with the Rmax unlinked by sensors, analyzed using the Octet data analysis software (ForteBio, version 9.0). Data shown are representative of three independent experiments.

highlight the critical role of the mutated residues in maintaining the pA104R−thonningianin A binding. It is noteworthy that K92, R94, and K97 have been identified as critical DNA-binding sites. Occupation of these sites by compound may prevent pA104R−DNA binding.

High-resolution crystal structure of apo pA104R: results from attempts to obtain a co-crystal with compound

After conducting a series of studies involving theoretical predictions, cell-free experiments, and cell-based assays to explore the binding mode between pA104R and thonningianin A, we proceeded with attempts to obtain a co-crystal structure using both soaking and co-crystallization methods. Unfortunately, no co-crystals were formed; however, we successfully obtained a high-resolution crystal structure of the apo form of pA104R (PDB ID 9JS5). The statistics for crystallographic data collection and structure refinement are listed in Supplementary Table 4. The crystalline form is consistent with the previously reported structure of pA104R (PDB ID 6LMH), sharing the same space group P2331, but with an improved resolution from 2.8 Å to 1.8 Å, which reveals more detailed structural features.

As shown in Figure 7(a), the overall structure of pA104R exists as a functional dimer, where the arm regions of the two monomers converge to form a clamp-like cavity, known as BDR. Each monomer of pA104R is composed of two alpha helices (α1 and α2), five beta sheets(β1-5), and a terminal alpha/3_10 helix (α3/η1) (Figure 7(b)). We then compared it with the previously reported structures of pA104R both in its ligand-free form (PDB ID 6LMH) and in complex with DNA (PDB ID 6LMJ). Figure 7(c) shows that the crystal structure of pA104R we resolved is highly consistent with the previously reported ligand-free form (coloured grey). The superimposition of these two structures shows a RMSD of 0.96 Å across 396 paired Cα atoms. However, when bound with DNA (coloured purple), the arm region of pA104R exhibits a noticeable inward bending of 19°, revealing its structural adaptability during the DNA binding process. The electrostatic surface of the pA104R indicated that the BDR is densely populated with positively charged amino acids (Figure 7(d)), which are crucial sites for binding to the negatively charged DNA. Notably, although no small molecules were observed in the BDR region, five sulfate ions identified, forming electrostatic interactions with positively charged amino acids (Figure 7(e)). Among these, K57，R69，K85，K92, and R94 were identified as a key residue for DNA binding.

MolProbity analysis identified a few poorly modelled residues, most of which are located at the N-terminus or on the α2 helix, distant from the DNA-binding region. In addition, minor atomic clashes were observed in the side chain of lysine residues (K92 and K97), likely due to their inherent flexibility, which presents challenges for precise modelling. Despite these minor geometric deviations, the residues are well-defined by electron density (RSCC > 0.85, RSRZ < 2), and the clash magnitudes remain low (clash magnitude < 1). Therefore, these minor structural anomalies are unlikely to affect the functional interpretation of pA104R.

We speculate that sulfate ions in the crystallization solution occupy binding sites that could otherwise accommodate small molecules, potentially disrupting their interactions with the protein. Therefore, we conducted further cocrystallization experiments using a sulfate-free crystallization buffer. Regrettably, this method still failed to yield the desired crystal structure of the complex. We suspect that the abundance of positively charged amino acids in the BDR region of pA104R structure may have hindered co-crystallization, ultimately preventing the formation of the complex. These findings highlight the inherent difficulty of crystallizing this protein in complex with small molecules, and further structural studies are necessary to overcome these obstacles.

Discussion

ASFV is highly contagious and causes fatal disease in domestic and wild pigs. To effectively control and prevent ASFV, it is essential to identify drug targets and develop efficacious treatments. pA104R is a crucial DNA-binding protein that plays a vital role in viral replication and progeny virus assembly, making it an ideal target for small-molecule inhibitors. Compounds that efficiently block pA104R−DNA binding hold promise for inhibiting ASFV replication. As reported by Liu et al., the stilbene derivatives SD1 and SD4 suppress ASFV replication by disrupting the binding between pA104R and DNA [17]. In this study, we employed a structure-based drug discovery approach combined with biological activity validation to identify ASFV pA104R inhibitors (Figure 1). For the first time, we reported that thonningianin A, isolated from an African medicinal herb, inhibits ASFV replication ex vivo in PAMs (IC$_{50}$ = 0.068 μM), and mechanistic studies suggest that this is accomplished by binding to the base of pA104R BDR (KD = 7.58 μM), thereby blocking the pA104R−DNA binding (Figures 2 and 3). This finding not only provides cost-efficient therapeutic candidates for ASFV therapy but also offers new insights into structure-based drug discovery.

To date, 24 ASFV genotypes have been identified, with genotype II being the most closely associated with the ongoing pandemic [53]. ASFV DNA polymerase X exhibits low fidelity due to the lack of 3′-5′ exonuclease proofreading activity [54], and DNA ligase further exacerbates errors during the repair process [55]. These factors result in a mutation rate much higher than that of conventional DNA viruses, complicating vaccine and drug design. Despite the presence of multiple ASFV variants, mutations are
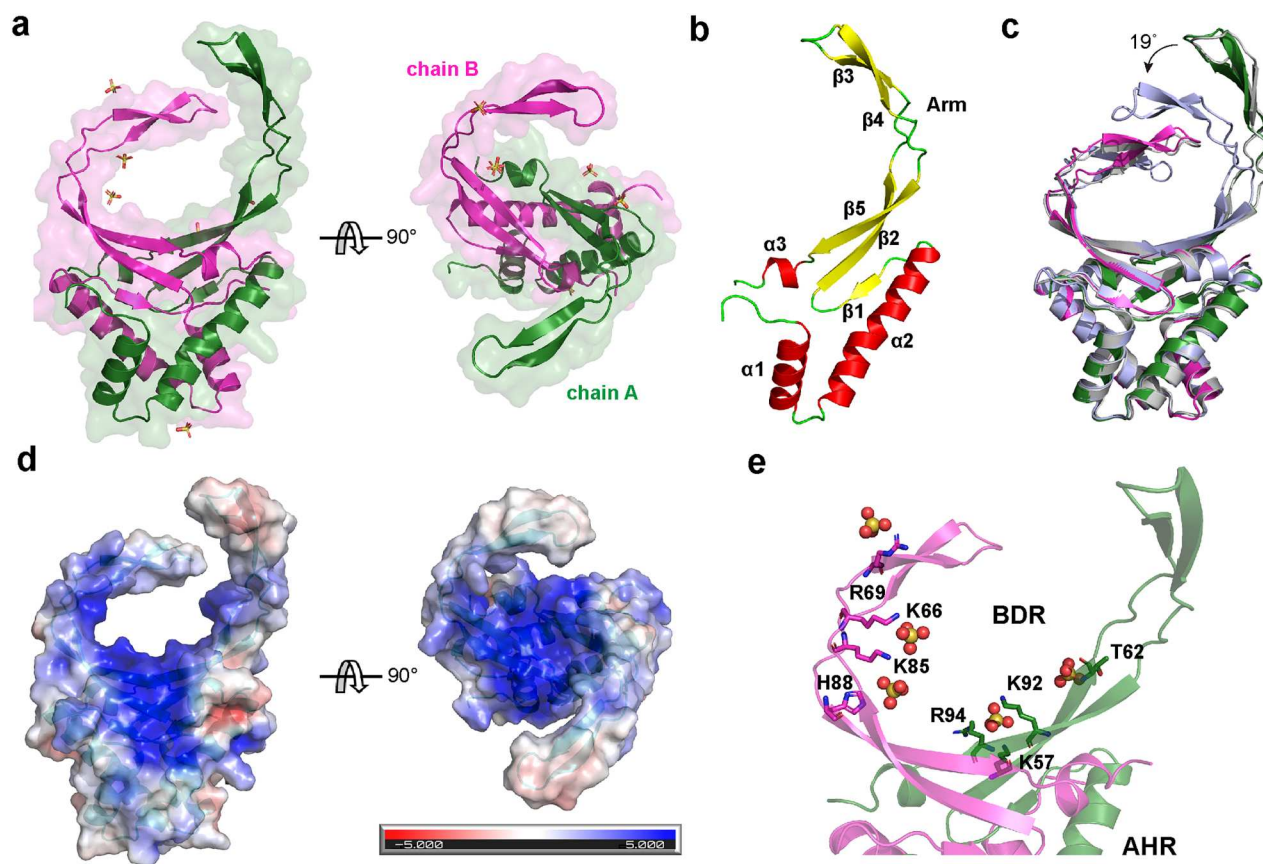
Figure 7. The x-ray structure of pA104R. a The overall structure of dimeric pA104R. **b** One protomer of the dimeric pA104R. **c** Structural superposition of for the pA104 (PDB ID 9JS5) with the previously reported structures of pA104R both in its ligand-free form (grey, PDB ID 6LMH) and in complex with DNA (light blue, PDB ID 6LMJ). **d** Surface electrostatic potential of pA104R. The electrostatic potential was calculated using the Adaptive Poisson-Boltzmann Solver (APBS) programme within the PyMOL environment. The calculations of the electrostatic potential were based on a pH of 7.5, with values ranging from −5 kT (red) to 5 kT (blue). **e** The sulfate ions in the BRD region of the crystal structure and their interacting residues. Sulfate ions are displayed as spheres, while amino acids are shown using the stick model. The PDB file was generated using molecular replacement, with residue numbering inherited from the template structure (PDB ID: 6LMH), which is offset by +6 relative to the NCBI reference sequence (Gen-Bank: AYW34006.1). For consistency with previous studies, residue numbering in the figures follows the NCBI reference sequence. The visualization and analysis of structures were conducted using the PyMOL Molecular Graphics System (version 3.0.0).

primarily concentrated in the left and right variable regions of the genome [8], while pA104R is located outside these variable regions. Roxas et al. analyzed 91 pA104R homologs across five distinct evolutionary clades and found that pA104R is highly conserved, especially in virulent ASFV strains [56]. Phylogenetic analysis revealed that the nucleotide substitution rate of pA104R is lower than that of other ASFV genes [18]. In this study, a multiple sequence alignment of pA104R across 8 genotypes revealed a high degree of conservation (Figure 5(h)), further highlighting its potential as a broad-spectrum target for anti-ASFV drug development.

Here, we reported the highest-resolution crystal structure of pA104R to date (Figure 7 and Supplementary Table 4), providing a structural basis for developing small-molecule inhibitors. The structure (PDB DB 9JS5) reveals a large, highly positively charged binding interfave, posing challenges in identifying effective inhibitors. In this context, structure-based virtual screening provides an efficient strategy for identifying

inhibitors from large compound libraries. Following the multi-layer screening strategy outlined in Figure 1, we identified two classes of small molecules: compound 1(evans blue), possessing four negative charges, may potentially engage in strong electrostatic interactions with positively charged amino acids in the BDR; compound 46 (thonningianin A), although is neutral, it is rich in polar groups such as hydroxyls, enabling effective binding to the BDR through hydrogen bonds and other polar interactions (Figure 5). Both compounds are anticipated to block the binding between pA104R and DNA by occupying the DNA-binding site. Subsequent in vitro antiviral assays confirmed their activity against ASFV, validating the effectiveness of our screening strategy (Figure 3).

Although these compounds demonstrated strong in vitro interaction with pA104R (Figure 2), our attempts at co-crystallization and soaking were unsuccessful in obtaining crystal structures of pA104R in complexed with these compounds. First, sulfate ions in the crystallization solution could form strong electrostatic

interactions with the positively charged residues, such as K92 and R94, occupying critical phosphate-binding sites (Figure 7). The presence of sulfate ions at these sites may interfere with the effective binding of the compond, preventing it from establishing a well-defined binding mode with pA104R. Furthermore, the relatively large binding cavity in the BDR region of pA104R may limit the ability of compound to fully occupy the binding sites. This incomplete occupancy may destabilize the complex within the crystallization environment, further obstructing the formation of a well-ordered crystal lattice. Furthermore, pA104R may need to undergo a certain degree of conformational changes to stably bind to thonningianin A. However, in the soaking experiment, the crystalline state imposes lattice constraints that may restrict the conformational flexibility required for effective ligand accommodation, thereby complicating the crystallization process. Given the challenges encountered in co-crystallization, we employed molecular docking and MD simulations to predict its binding site on pA104R (Figure 5). The top ten residues that contribute most to the binding free energy of thonningianin A are H100, V61, A90, A95, V63, K92, L96, R94, K97, and V99 (Figure 5(g)). These residues were further validated through site-directed mutagenesis experiments, where mutations to D or A significantly weakened the affinity of the compounds for pA104R (Figure 6). While we have identified several key binding sites, the lack of co-crystallization, which would provide the most direct evidence, suggests that the binding mechanism may involve complex dynamic processes or specific conformational changes that require further studies.

Thonningianin A, the methanol extract of the African medicinal herb (thonningia sanguinea), has shown a broad spectrum of pharmacological effects, including antioxidant [57], antibacterial [58], antihyperglycemic [59], anticancer [60], and neuroprotective properties [61]. Notably, we have discovered that thonningianin A also exhibits anti-ASFV activity in vitro. Pharmacokinetic studies of thonningianin A in rats, as reported by Liu et al., reveals that at a dose of 10 mg/kg, this compound is rapidly absorbed (Tmax 0.83 h), reaches a moderate maximum plasma concentration (Cmax 221.9 ng/mL), and has a relatively long half-life ($t_{1/2}$ 3.69 h) [62]. These findings suggest that thonningianin A exhibits both efficient absorption and sustained action in rats. Notably, It is crucial to consider cost-effectiveness when developing veterinary medicines. Medicinal plants are gaining increasing recognition worldwide for their low cost and characteristic benefits. Compared to chemically synthesized compounds, the development of Herbal drugs which are cost-effective and can be scaled up through sustainable cultivation and harvesting. Therefore, thonningianins A, with its favourable pharmacokinetic properties, safety, and cost-effectiveness, may have the potential to be developed as anti-ASFV drug.

ASFV DNA packaging is a dynamic process involving the collaboration of multiple proteins [14]. In the current study, while evidence suggests that thonningianin A does not affect the structural stability of pA104R in silico or its expression levels in cells, we cannot exclude the possibility that the compound may influence other functional aspects of pA104R. For example, the synergy effect between pA104R and pP1192R, which induce DNA supercoiling and ultimately leads to the formation of mature viral particles [63,64]. Additionally, given the complexity of ASFV replication, which involves multiple viral proteins and host factors, the possibility of other potential targets cannot be excluded. Although our study found that thonningianin A did not significantly affect IFNα/β mRNA expression levels, influenza virus replication, or ASFV protease activity (data not shown), the existence of other potential inhibitory mechanisms warrants further investigation.

Conclusion

In summary, this study demonstrates the in vitro anti-ASFV activity of thonningianin A. Moreover, thonningianin A binds to the bottom of the BDR region of pA104R, occupying key DNA-binding sites and blocking the pA104R−DNA binding, thereby inhibiting viral replication. Given the high conservation of pA104R across different strains, small-molecule inhibitors targeting this protein have the potential for broad-spectrum antiviral activity. Moreover, thonningianin A is derived from an African medicinal herb, it presents a cost-effective and promising drugs for anti-ASFV. Although inhibitory effects of thonningianin A against ASFV has not yet been confirmed in vivo, its potential as an economical and effective inhibitor offers a promising option for the development of anti-ASFV drugs.

Acknowledgements

Author contributions

Quan-jie Li performed the structure-based virtual screening, conducted molecular modelling, and analyzed the structures. Hui-han Shao was responsible for protein expression and purification, along with performing EMSA and PLA assays. Lin-lin Zheng

evaluated the inhibitory effects of compounds on viral replication at the cellular level. Qian Liu and Chenchao Huo evaluated the binding kinetics and cytotoxicity of compounds. Shan Cen, Quan-jie Li, Dongrong Yi, and Tao Feng conceived and supervised this study. Quan-jie Li wrote the manuscript. Shan Cen revised the manuscript. All authors participated in the discussion and editing of the manuscript.

Disclosure statement

Funding

Data availability

The atomic coordinate of pA104R has been deposited in the Protein Data Bank, https://www.wwpdb.org/, under accession code 9JS5.

References

[1] Dixon L, Sun H, Roberts H. African swine fever. Antiviral Res. 2019;165:34–41. doi:10.1016/j.antiviral.2019.02.018

[2] Li Z, Chen W, Qiu Z, et al. African swine fever virus: a review. Life. 2022;12(8):1255. doi:10.3390/life12081255

[3] Ata EB, Li Z-J, Shi C-W, et al. African swine fever virus: a raised global upsurge and a continuous threaten to pig husbandry. Microb Pathog. 2022;167:105561. doi:10.1016/j.micpath.2022.105561

[4] Urbano AC, Ferreira F. African swine fever control and prevention: an update on vaccine development. Emerg Microbes Infect. 2022;11(1):2021–2033. doi:10.1080/22221751.2022.2108342

[5] Chandana M, Nair SS, Chaturvedi V, et al. Recent progress and major gaps in the vaccine development for African swine fever. Braz J Microbiol. 2024;55(1):997–1010. doi:10.1007/s42770-024-01264-7

[6] Borca MV, Ramirez-Medina E, Silva E, et al. Development of a highly effective African swine fever virus vaccine by deletion of the I177L gene results in sterile immunity against the current epidemic Eurasia strain. J Virol. 2020;94(7):e02017-19. doi:10.1128/JVI.02017-19

[7] Sánchez-Vizcaíno JM, Laddomada A, Arias ML. African swine fever virus. In: Zimmerman JJ, Karriker LA, Ramirez A, et al., editors. Diseases of swine. 11th ed. New York: Wiley; 2019. p. 443–452.

[8] Dixon LK, Chapman DA, Netherton CL, et al. African swine fever virus replication and genomics. Virus Res. 2013;173(1):3–14. doi:10.1016/j.virusres.2012.10.020

[9] Wang N, Zhao D, Wang J, et al. Architecture of African swine fever virus and implications for viral assembly. Science. 2019;366(6465):640–644. doi:10.1126/science.aaz1439

[10] Liu S, Luo Y, Wang Y, et al. Cryo-EM structure of the African swine fever virus. Cell Host Microbe. 2019;26(6):836–843.e3. doi:10.1016/j.chom.2019.11.004

[11] Liu Q, Ma B, Qian N, et al. Structure of the African swine fever virus major capsid protein p72. Cell Res. 2019;29(11):953–955. doi:10.1038/s41422-019-0232-x

[12] Wang G, Xie M, Wu W, et al. Structures and functional diversities of ASFV proteins. Viruses. 2021 Oct 21;13(11):2124. doi:10.3390/v13112124

[13] Fu D, Zhao D, Zhang W, et al. Structure of African swine fever virus p15 reveals its dual role for membrane-association and DNA binding. Protein Cell. 2020 Aug;11(8):606–612. doi:10.1007/s13238-020-00731-9

[14] Urbano AC, Ferreira F. Role of the DNA-binding protein pA104R in ASFV genome packaging and as a novel target for vaccine and drug development. Vaccines (Basel). 2020 Oct 3;8(4):585. doi:10.3390/vaccines8040585

[15] Frouco G, Freitas FB, Coelho J, et al. DNA-Binding Properties of African swine fever virus pA104R, a histone-like protein involved in viral replication and transcription. J Virol. 2017 Jun 15;91(12):e02498-16. doi:10.1128/JVI.02498-16

[16] Borca M, Irusta P, Kutish G, et al. A structural DNA binding protein of African swine fever virus with similarity to bacterial histone-like proteins. Arch Virol. 1996;141:301–313. doi:10.1007/BF01718401

[17] Liu R, Sun Y, Chai Y, et al. The structural basis of African swine fever virus pA104R binding to DNA and its inhibition by stilbene derivatives. Proc Natl Acad Sci USA. 2020 May 19;117(20):11000–11009. doi:10.1073/pnas.1922523117

[18] Urbano AC, Ferreira N, Jordão N, et al. Targeted mutagenesis of the β-strand DNA binding region of African swine fever virus histone-like protein (pA104R) impairs DNA-binding activity and antibody recognition. Antiviral Res. 2024 Jan;221:105784. doi:10.1016/j.antiviral.2023.105784

[19] Chen Q, Li L, Guo S, et al. African swine fever virus pA104R protein acts as a suppressor of type I interferon signaling. Front Microbiol. 2023;14:1169699. doi:10.3389/fmicb.2023.1169699

[20] Freitas FB, Simões M, Frouco G, et al. Towards the generation of an ASFV-pA104R DISC mutant and a complementary cell line-A potential methodology for the production of a vaccine candidate. Vaccines (Basel). 2019 Jul 18;7(3):68. doi:10.3390/vaccines7030068

[21] Ramirez-Medina E, Vuono EA, Pruitt S, et al. Deletion of African swine fever virus histone-like protein, A104R from the Georgia isolate drastically reduces virus virulence in domestic pigs. Viruses. 2022;14(5):1112. doi:10.3390/v14051112

[22] Galindo I, Hernáez B, Berná J, et al. Comparative inhibitory activity of the stilbenes resveratrol and oxyresveratrol on African swine fever virus replication. Antiviral Res. 2011;91(1):57–63. doi:10.1016/j.antiviral.2011.04.013

[23] Guo S, Zhang Y, Liu Z, et al. Brincidofovir is a robust replication inhibitor against African swine fever virus in vivo and in vitro. Emerg Microbes Infect. 2023;12(2):2220572. doi:10.1080/22221751.2023.2220572

[24] Goulding LV, Kiss E, Goatley L, et al. In vitro and in vivo antiviral activity of nucleoside analogue cHPMPC against African swine fever virus replication. Antiviral Res. 2022;208:105433. doi:10.1016/j.antiviral.2022.105433

[25] Li T, Zheng J, Huang T, et al. Identification of several African swine fever virus replication inhibitors by screening of a library of FDA-approved drugs. Virology. 2024;593:110014. doi:10.1016/j.virol.2024.110014

[26] Freitas FB, Frouco G, Martins C, et al. In vitro inhibition of African swine fever virus-topoisomerase II disrupts viral replication. Antiviral Res. 2016;134:34–41. doi:10.1016/j.antiviral.2016.08.021

[27] Mottola C, Freitas FB, Simões M, et al. In vitro antiviral activity of fluoroquinolones against African swine fever virus. Vet Microbiol. 2013;165(1-2):86–94. doi:10.1016/j.vetmic.2013.01.018

[28] Chen Y, Guo Y, Chang H, et al. Brequinar inhibits African swine fever virus replication in vitro by activating ferroptosis. Virol J. 2023;20(1):242. doi:10.1186/s12985-023-02204-x

[29] Grigoryan R, Arabyan E, Izmailyan R, et al. Antiviral activity of brequinar against African swine fever virus infection in vitro. Virus Res. 2022;317:198826. doi:10.1016/j.virusres.2022.198826

[30] Zhao Y, Niu Q, Yang S, et al. Inhibition of BET family proteins suppresses African swine fever virus infection. Microbiol Spectr. 2022;10(4):e02419-21. doi:10.1128/spectrum.02419-21

[31] Gao Q, Yang Y, Feng Y, et al. Effects of the NF-κB signaling pathway inhibitor BAY11-7082 in the replication of ASFV. Viruses. 2022;14(2):297. doi:10.3390/v14020297

[32] Liu B, Cui Y, Lu G, et al. Small molecule inhibitor E-64 exhibiting the activity against African swine fever virus pS273R. Bioorg Med Chem. 2021;35:116055. doi:10.1016/j.bmc.2021.116055

[33] De León P, Bustos MJ, Torres E, et al. Inhibition of porcine viruses by different cell-targeted antiviral drugs. Front Microbiol. 2019;10:1853. doi:10.3389/fmicb.2019.01853

[34] Chen Y, Wei Z, Song Z, et al. Theaflavin inhibits African swine fever virus replication by disrupting lipid metabolism through activation of the AMPK signaling pathway in virto. Virus Res. 2023;334:199159. doi:10.1016/j.virusres.2023.199159

[35] Qian B, Hu Y, Liu C, et al. Tetrandrine (TET) inhibits African swine fever virus entry into cells by blocking the PI3 K/Akt pathway. Virus Res. 2024;339:199258. doi:10.1016/j.virusres.2023.199258

[36] Chen Y, Song Z, Chang H, et al. Dihydromyricetin inhibits African swine fever virus replication by downregulating toll-like receptor 4-dependent pyroptosis in vitro. Vet Res. 2023;54(1):58. doi:10.1186/s13567-023-01184-8

[37] Hakobyan A, Arabyan E, Kotsinyan A, et al. Inhibition of African swine fever virus infection by genkwanin. Antiviral Res. 2019;167:78–82. doi:10.1016/j.antiviral.2019.04.008

[38] Arabyan E, Hakobyan A, Hakobyan T, et al. Flavonoid library screening reveals kaempferol as a potential antiviral agent against African swine fever virus. Front Microbiol. 2021;12:736780. doi:10.3389/fmicb.2021.736780

[39] Arabyan E, Hakobyan A, Kotsinyan A, et al. Genistein inhibits African swine fever virus replication in vitro by disrupting viral DNA synthesis. Antiviral Res. 2018;156:128–137. doi:10.1016/j.antiviral.2018.06.014

[40] Lv C, Yang J, Zhao L, et al. Bacillus subtilis partially inhibits African swine fever virus infection in vivo and in vitro based on its metabolites arctiin and genistein interfering with the function of viral topoisomerase II. J Virol. 2023;97(11):e00719-23. doi:10.1128/jvi.00719-23

[41] Jo S, Kim S, Shin DH, et al. Inhibition of African swine fever virus protease by myricetin and myricitrin. J Enzyme Inhib Med Chem. 2020;35(1):1045–1049. doi:10.1080/14756366.2020.1754813

[42] Hakobyan A, Arabyan E, Avetisyan A, et al. Apigenin inhibits African swine fever virus infection in vitro. Arch Virol. 2016;161:3445–3453. doi:10.1007/s00705-016-3061-y

[43] Zhang Y, Zhang Z, Zhang F, et al. ASFV transcription reporter screening system identifies ailanthone as a broad antiviral compound. Virol Sin. 2023;38(3):459–469. doi:10.1016/j.virs.2023.03.004

[44] Hurtado C, Bustos MJ, Sabina P, et al. Antiviral activity of lauryl gallate against animal viruses. Antivir Ther. 2008;13(7):909–917. doi:10.1177/135965350801300704

[45] Jackman JA, Hakobyan A, Grigoryan R, et al. Antiviral screening of natural, anti-inflammatory compound library against African swine fever virus. Virol J. 2024;21(1):95. doi:10.1186/s12985-024-02374-2

[46] Ekor M. The growing use of herbal medicines: issues relating to adverse reactions and challenges in monitoring safety. Front Pharmacol. 2014;4:177. doi:10.3389/fphar.2013.00177

[47] Huey R, Morris GM, Forli S. Using AutoDock 4 and AutoDock Vina with AutoDockTools: a tutorial. Scripps Res Inst Mol Graphics Lab. 2012;10550(92037):1000.

[48] O'Boyle NM, Banck M, James CA, et al. Open babel: An open chemical toolbox. J Cheminform. 2011;3:1–14. doi:10.1186/1758-2946-3-1

[49] Trott O, Olson AJ. Autodock Vina: improving the speed and accuracy of docking with a new scoring function, efficient optimization, and multithreading. J Comput Chem. 2010;31(2):455–461. doi:10.1002/jcc.21334

[50] Adams PD, Afonine PV, Bunkóczi G, et al. PHENIX: a comprehensive python-based system for macromolecular structure solution. Acta Crystallogr Sect D: Biol Crystallogr. 2010;66(2):213–221. doi:10.1107/S0907444909052925

[51] Emsley P, Cowtan K. Coot: model-building tools for molecular graphics. Acta Crystallogr Sect D: Biol Crystallogr. 2004;60(12):2126–2132. doi:10.1107/S0907444904019158

[52] Nidavani RB, Mahalakshmi A, Shalawadi M. Vascular permeability and evans blue dye: a physiological and pharmacological approach. J Appl Pharm Sci. 2014;4(11):106–113. doi:10.7324/JAPS.2014.41119

[53] Qu H, Ge S, Zhang Y, et al. A systematic review of genotypes and serogroups of African swine fever virus. Virus Genes. 2022;58(2):77–87. doi:10.1007/s11262-021-01879-0

[54] García-Escudero R, García-Díaz M, Salas M, et al. DNA polymerase X of African swine fever virus: insertion fidelity on gapped DNA substrates and AP lyase activity support a role in base excision repair of viral DNA. J Mol Biol. 2003;326(5):1403–1412. doi:10.1016/s0022-2836(03)00019-6

[55] Chen Y, Liu H, Yang C, et al. Structure of the error-prone DNA ligase of African swine fever virus identifies critical active site residues. Nat Commun. 2019 Jan 23;10(1):387. doi:10.1038/s41467-019-08296-w

[56] Roxas TJR, Gomez MC, Tayo LL. Phylogenetic analysis of the histone-like protein (pA104R) reveals high conservation among African swine fever virus (ASFV) variants. Proceedings of the 9th International Conference on Bioinformatics Research and Applications, Association for Computing Machinery, New York, NY, USA. 2023. p. 6-13. doi:10.1145/3569192.3569194

[57] Gyamfi MA, Aniya Y. Antioxidant properties of thonningianin A, isolated from the African medicinal herb, thonningia sanguinea. Biochem Pharmacol. 2002;63(9):1725–1737. doi:10.1016/s0006-2952(02)00915-2

[58] Wang H, Li H, Liu Z, et al. Activity of thonningianin A against Candida albicans in vitro and in vivo. Appl Microbiol Biotechnol. 2024;108(1):96. doi:10.1007/s00253-023-12996-1

[59] Shen J, Zhang C, Liu Y, et al. L-type calcium ion channel-mediated activation of autophagy in vascular smooth muscle cells via thonningianin A (TA) alleviates vascular calcification in type 2 diabetes mellitus. Eur J Pharmacol. 2023;959:176084. doi:10.1016/j.ejphar.2023.176084

[60] Zhang T-T, Yang L, Jiang J-G. Effects of thonningianin A in natural foods on apoptosis and cell cycle arrest of HepG-2 human hepatocellular carcinoma cells. Food Funct. 2015;6(8):2588–2597. doi:10.1039/c5fo00388a

[61] Zhou X-G, Qiu W-Q, Yu L, et al. Targeting microglial autophagic degradation of the NLRP3 inflammasome for identification of thonningianin A in Alzheimer's disease. Inflamm Regen. 2022;42(1):25. doi:10.1186/s41232-022-00209-7

[62] Liu Q, Li C, Zhao P, et al. Quantification of thonningianin a in rat plasma by liquid chromatography tandem mass spectrometry and its application to a pharmacokinetic study. Pharm Biol. 2021;59(1):523–529. doi:10.1080/13880209.2021.1913188

[63] Coelho J, Ferreira F, Martins C, et al. Functional characterization and inhibition of the type II DNA topoisomerase coded by African swine fever virus. Virology. 2016;493:209–216. doi:10.1016/j.virol.2016.03.023

[64] Cong J, Xin Y, Kang H, et al. Structural insights into the DNA topoisomerase II of the African swine fever virus. Nat Commun. 2024;15(1):4607. doi:10.1038/s41467-024-49047-w